

# RFI Detection and Mitigation for Microwave Radiometry With an Agile Digital Detector

Christopher S. Ruf, *Fellow, IEEE*, Steven M. Gross, and Sidharth Misra

**Abstract**—A new type of microwave radiometer detector has been developed that is capable of identifying high and low levels of radio-frequency interference (RFI) and of reducing or eliminating its effect on the measured brightness temperatures. High-level, localized RFI can be easily identified by its unnatural appearance in brightness temperature imagery. Low-level or persistent RFI can be much more difficult to identify and filter out. The agile digital detector (ADD) can discriminate between RFI and natural thermal emission signals by directly measuring higher order moments of the signal than the variance that is traditionally measured. After detection, the ADD then uses spectral filtering methods to selectively remove the RFI. ADD performance is experimentally verified in controlled laboratory tests and in the field near a commercial air traffic control radar. High-level RFI is easily identified and removed. Very low level RFI contamination, with power levels as low as the radiometric measurement uncertainty of the radiometer, is also shown to be reliably detected and removed.

**Index Terms**—Microwave radiometry, radio spectrum management.

## I. INTRODUCTION

RECENT experience with the C-band channel on the Advanced Microwave Scanning Radiometer (AMSR-E) indicates that the potential exists for a very serious deterioration in the quality of soil moisture science products produced by a spaceborne microwave radiometer as a result of radio-frequency interference (RFI) [9], [12]. Even L-band radiometers operating in the “protected” frequency band surrounding the 21-cm hydrogen line have been subject to significant RFI in aircraft campaigns [7], [8]. One previous effort to detect and mitigate the presence of RFI in microwave radiometers consists of replacing the standard analog detector by a parallel bank of analog subband filters and detectors. This permits relatively high levels of narrowband RFI to be easily detected and removed [2]. The upcoming NPOESS Conical Microwave Imager Sounder spaceborne radiometer is considering using such an approach to mitigate RFI in its C-band channel [13]. The approach will have greater difficulty with the detection or removal of low level, broadband, and/or persistent sources of RFI.

With a simple parallel bank of filters, low level, broadband, and/or persistent RFI sources are difficult if not impossible to distinguish from natural variability in the geophysical parameter of interest. Without this detection capability, science quality

will be adversely impacted in two regards. First and most obviously, hot brightness temperature ( $T_B$ ) artifacts will be introduced into the image. For the case of soil moisture, the result is a shift in level of the retrieved soil moisture toward drier conditions [11]. This would, for example, result in an underestimation of the level of saturation of the land surface and, hence, an underestimation of the potential for flooding as a result of extreme precipitation events. In weather forecasting applications, underestimation of soil moisture results in lowered forecast cloud production and reduced accounting for latent heat transferred to the atmosphere from surface heating [1]. In addition to the detrimental effects RFI will have on short-term forecasting and flood prediction, it also affects the quality of long-term climatological measurements. This results because RFI is inherently a positive bias to observed  $T_B$ . As such, its impact on geophysical parameter retrievals will not “average down” over time as do many other sources of error. As a result, even low levels of RFI—levels that might not be large enough to introduce significant errors into short-term applications such as weather forecasting—are of great concern. However, it is precisely the low-level RFI that is most likely to escape detection by conventional filter bank methods.

Attempts have also been made to detect and mitigate the presence of RFI in radiometers using digital signal processing [4]. The approach is similar to that in the analog case but performance is improved by increasing the spectral and/or the temporal resolution of the samples. In both the analog and digital cases, however, there is still a problem with detection of low-level RFI that raises the  $T_B$  by an amount that is not distinguishable from the variability of the naturally occurring thermal emission.

An agile digital detector (ADD) has been developed that is capable of performing the standard functions of a conventional analog detector, the more advanced functions of an analog bank of subband filters and detectors, as well as an entirely new class of radiometer detection and mitigation algorithms that are optimized for the removal of low-level RFI contamination of microwave radiometer  $T_B$ . The essential elements of the ADD hardware consist of a high-speed, high-resolution analog-to-digital converter (ADC), followed by a field-programmable gate array (FPGA) to perform digital signal processing (DSP) functions (see Fig. 1). Analog radiometer signals enter the ADD in place of what would ordinarily be the detection stage of the hardware. The DSP stage of the ADD provides direct measurements of the probability density function (pdf) of the predetection signal. The pdf can be used, in ways described in the following sections, to detect the presence of RFI. The ADD should be considered as a potential replacement for the simple analog

Manuscript received July 7, 2005; revised September 20, 2005. This work was supported in part by the NASA Goddard Space Flight Center and its Earth Science Technology Office under Grants NNG05GB08G and NNG05GL97G.

The authors are with the Space Physics Research Laboratory, Department of Atmospheric, Oceanic, and Space Sciences, University of Michigan, Ann Arbor, 48109 MI USA (e-mail: cruf@umich.edu).

Digital Object Identifier 10.1109/TGRS.2005.861411

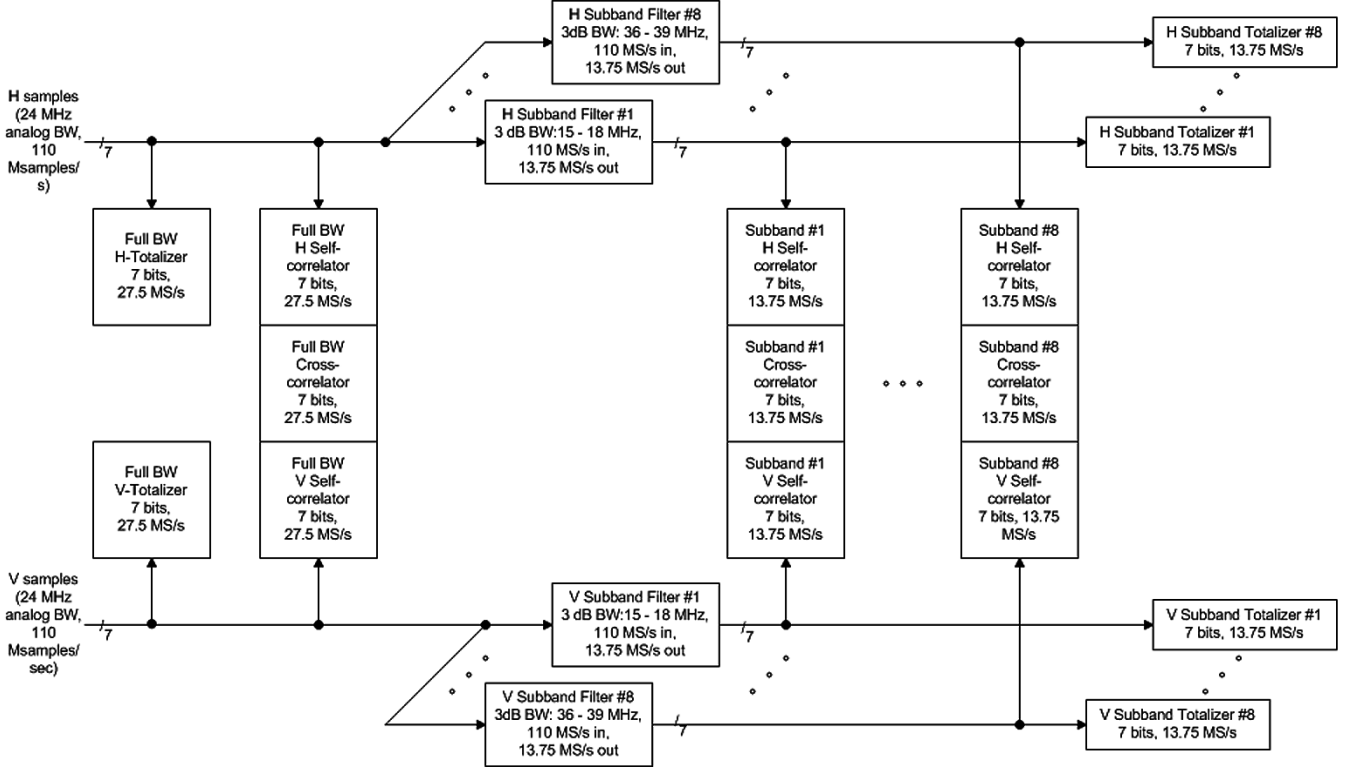


Fig. 1. Functional block diagram of ADD digital signal processing.

detector scheme that has historically been used by nearly all previous airborne and spaceborne microwave radiometers.

## II. THEORY OF OPERATION

Radiometer signals are generated by noise and so are inherently random processes. In the absence of RFI, the predetection analog signal in a microwave radiometer is generated exclusively by thermal emission sources. These sources include both the natural thermal emission incident on the antenna from the Earth and sky as well as the radiometer noise generated by ohmic losses and noisy active components in the hardware. In this case, the pdf of the amplitude of the signal is Gaussian distributed. Signal sources other than thermal noise will, in almost all cases, have non-Gaussian pdfs. Leveraging this fact is the basis for the ADD theory of operation.

The  $T_B$  measured by a radiometer is related to its predetection signal,  $x(t)$ , by

$$T_B = G \langle x^2(t) \rangle \quad (1)$$

where the constant of proportionality,  $G$ , represents the radiometer gain. The expectation operation in (1) can be expanded as

$$\langle x^2(t) \rangle = \int_{-\infty}^{+\infty} x^2 p(x) dx \quad (2)$$

where  $p(x)$  is the pdf of  $x$ . In other words, the  $T_B$  is proportional to the second moment of the predetection analog signal. (We assume that  $x(t)$  is a zero-mean signal. In practice, any constant offset is measured and subtracted.) A conventional analog

square-law detector estimates  $T_B$  by measuring a time average of the square of the signal, or

$$T_{B\_analog} = G \left[ \frac{1}{\tau} \int_{t-\tau}^t x^2(t') dt' \right] \quad (3)$$

where  $\tau$  is the integration time. Rather than measuring a time average of  $x^2(t)$  directly, the ADD measures  $p(x)$ , the pdf of  $x$ . It does so by counting numbers of occurrences of each quantization level of the digitized predetection signal. This histogram of the amplitude of  $x(t)$  is essentially a discrete version of  $p(x)$ . For the ADD, the discrete pdf itself becomes the raw, Level 0, data product that is recorded for subsequent postprocessing. Determination of the second moment and, hence, of the  $T_B$  by conventional means becomes a part of the Level 1 postprocessing. Specifically, the  $T_B$  is computed by

$$T_{B\_ADD} = G \left[ \frac{1}{N} \sum_{i=1}^M q^2(i) p(i) \right] \quad (4)$$

where  $N$  is the total number of samples in the discrete pdf,  $M$  is the total number of quantization bins,  $q(i)$  is the amplitude of the  $i$ th quantization bin, and  $p(i)$  is the number of samples that fell in the  $i$ th quantization bin. The radiometer gain,  $G$ , would be determined via end-to-end system calibration in the same manner as for the analog case. It should be noted that this approach to square-law detection has been successfully implemented previously by the X-band Lightweight Rainfall Radiometer [14].

The ADD approach makes the discrete pdf of the predetection signal available for postprocessing. This opens up an entirely new class of radiometer signal processing options for the

detection of RFI. Specifically, an analog square-law detector simply measures the power present in the signal. Low-level RFI will raise the power and, hence, the  $T_B$  estimated using (3), by a small amount. There is no independent way that the presence of RFI can be ascertained from this measurement. In the ADD case, on the other hand, the measured pdf will be perturbed away from a Gaussian distribution if the pdf of the RFI is non-Gaussian. It should be noted that man made interference having a Gaussian or near-Gaussian distribution would be difficult if not impossible to detect using the ADD method.

One algorithm for detecting RFI makes use of the generating function for higher order moments of a Gaussian distribution. The generating function is given by

$$\langle x^n(t) \rangle = 1 \cdot 3 \cdot \dots \cdot (n-1) \sigma^n, \quad \text{for } n \text{ even} \quad (5)$$

where  $\sigma$  is the standard deviation of  $x$ . It is important to note that all higher order moments of a Gaussian distributed random process are uniquely determined by its standard deviation. An RFI detection threshold can be constructed using (5). For example, the kurtosis of  $x$  is given by the ratio

$$R = \frac{\langle x^4(t) \rangle}{\langle x^2(t) \rangle^2} \quad (6)$$

and should equal exactly three if  $x(t)$  is Gaussian distributed, i.e., if it is a thermal noise signal that is free of RFI. This ratio is a robust test for RFI in the sense that it will not change as the brightness temperature varies but it will change if non-Gaussian distributed interference is introduced. Experimental evidence of this is presented in Section IV below. An examination of the dependence of the ratio on a particular class of RFI signals is discussed in Section V.

In practice, the expectation operations in (6) are approximated using a finite number of samples of  $x$ . This will introduce uncertainty into the estimator. The uncertainty has the same statistical origin as does the radiometer noise-equivalent delta-T ( $NE\Delta T$ ) uncertainty associated with estimates of the variance. In our case, there is an  $NE\Delta R$  corresponding to the uncertainty in estimating  $R$ . The error in estimating the kurtosis of a Gaussian distributed random variable from a finite number of samples,  $N$ , has been considered previously [5]. The standard deviation of the estimate is given by

$$NE\Delta R = \sqrt{\frac{24}{N}}. \quad (7)$$

For the case of radiometric observations, the number of samples,  $N$ , can be replaced by the product of the signal bandwidth,  $B$ , and the available integration time,  $\tau$ . The  $NE\Delta R$  sets a practical limit on the detectability threshold of low-level RFI. In the experimental results presented below, in Section IV, air traffic control radar RFI signals with equivalent brightness temperatures that are comparable in magnitude to the radiometer  $NE\Delta T$  are found to be reliably detectable.

### III. ADD IMPLEMENTATION DETAILS

#### A. Interface to Radiometer Front End

A prototype of the ADD has been designed, fabricated, and laboratory and field tested after integration with an existing L-band radiometer. Signal flow through the radiometer begins with a  $20^\circ$  half power beamwidth dual linear polarized horn antenna, followed by a single-pole double-throw calibration switch (that selects between the antenna and an ambient matched load), a directional coupler (that allows a calibration noise diode signal to be injected), a low-noise amplifier, more gain stages, and an RF band definition filter. The RF bandwidth of 24 MHz is centered on 1413.5 MHz. After the gain and band definition stages, the RF passband is downconverted to an intermediate frequency (IF) range of 15–39 MHz. The ADD backend then samples the IF signal at 110 MHz with a seven-bit signed digitizer. The samples are passed to an FPGA-based DSP module that performs subband filtering, correlations, and histogram digital signal processing. Individual samples of the histograms are generated from 36-ms integration periods. A periodic calibration sequence is followed in which nine antenna samples are taken, followed by one antenna + noise diode sample, followed again by nine antenna and then one antenna + noise diode samples. Next, nine samples of the reference load are taken, then one of the reference load plus noise diode, then again nine reference and one reference + noise diode samples. This sequence of 40 samples is repeated indefinitely. The complete sequence requires 1.458 s to complete, which is slightly more than  $40 \times 36$  ms to allow for settling time between state transitions.

#### B. Field-Programmable Gate Array Design

The ADD FPGA is implemented in a Xilinx Virtex-II Pro gate array. It samples the H-polarization and V-polarization analog channels at 110 megasamples/s, providing seven-bit signed representations of the sampled input to the downstream processing stages. The discrete pdf of each full-bandwidth input is calculated in the full-bandwidth totalizers. The power level of each input, as well as the cross-polarization power level, are calculated in the full-bandwidth correlators.

Each full-bandwidth polarization channel is processed by eight bandpass filters in parallel to divide the 24-MHz input bandwidth into discrete 3-MHz subbands. These filters are efficiently implemented as polyphase finite impulse response (FIR) decimators, taking advantage of the output bandwidth reduction to allow a factor-of-eight reduction in the output sample rate and a corresponding reduction in FPGA resource utilization [3]. The discrete (seven-bit) pdf of each of the eight subbands for both H-polarization and V-polarization is calculated in the subband totalizers, as is done with the full-bandwidth inputs. The power level for each subband, as well as the X-polarization power level, is also calculated in the subband correlators.

Every 36 ms, the FPGA initiates a readout operation, during which all of the integrated quantities (pdfs and power levels) are transferred to a command and data handling computer to be recorded for offline analysis. In addition to performing these functions, the FPGA also controls the instrument calibration state, switching between the antenna input and reference load

TABLE I  
REQUIREMENTS FOR ADD DIGITAL FILTER BANK

Total Bandwidth	24 MHz
Total Bandwidth range	15 MHz — 39 MHz
No. of channels	8
Bandwidth of each channel	3 MHz
Sampling Frequency	110 MHz
Number of taps	47
Pass band attenuation (normalized)	0 dB
Stop band attenuation (normalized)	> 40 dB
Coefficient resolution	9 bit signed

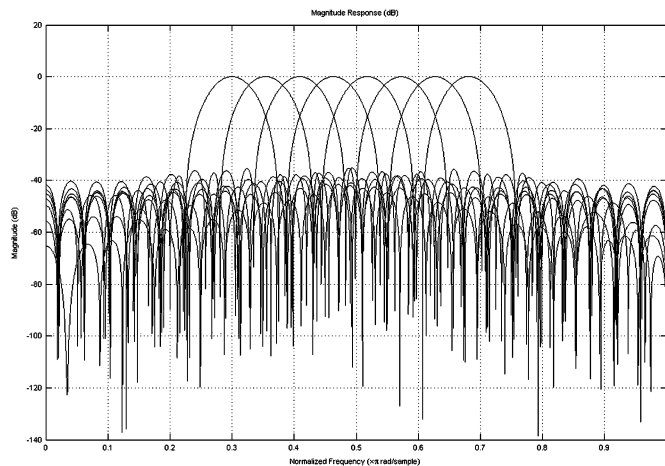


Fig. 2. Predicted transfer function of ADD filter banks using a Kaiser  $\beta = 3.2$  window with 47 taps and nine-bit signed coefficients.

and enabling the noise diode in a specified pattern. The cal state switching is synchronized with the readout to simplify calibration.

### C. Subband Digital Filter Design

The specific FPGA chosen is a midrange commercial part that allowed implementation of an eight-channel/47-tap design with nine-bit coefficients for the subband definition filter bank. Larger FPGAs are commercially available which would provide increased signal processing capacity (more channels, longer taps, and/or larger coefficients). Various design windows were considered for the filters such as Blackman–Harris, Hamming, Hanning, Gaussian, Kaiser, Equiripple, and Chebyshev. The main criteria for choosing the filter were a low stop band floor and minimum intersection between the channels. Kaiser window and Equiripple filter banks offer the most satisfactory performance for the given number of taps, channels, and number of bits used per coefficient. A summary of the filter requirements is given in Table I.

The Kaiser filter was chosen for development of the ADD prototype. In general, this filter has two parameters, the number of taps and the shape parameter  $\beta$  [10]. In our case the number of taps is fixed. The  $\beta$  parameter controls the width of the passband and the level of out-of-band rejection. For the present application, a value of  $\beta = 3.2$  was selected. Fig. 2 shows the resulting projected frequency response of the filter bank.

The out-of-band rejection between channels of the filter is summarized in Table II, which gives the maximum sensitivity of channels 1 and 4 to out-of-band signals with frequencies in each of the eight channels. Interfering signals in adjacent channels

TABLE II  
OUT-OF-BAND REJECTION (DECIBELS) BETWEEN CHANNELS OF THE ADD FILTER BANK USING KAISER  $\beta = 3.2$  WINDOW WITH NINE-BIT SIGNED COEFFICIENTS

Out-of-Band rejection (dB)	Ch1	Ch2	Ch3	Ch4	Ch5	Ch6	Ch7	Ch8
relative to Channel 1	0	3.10	16.08	39.72	39.51	38.44	43.64	41.25
relative to Channel 4	38.81	14.63	3.10	0	3.02	15.85	37.33	39.11

are reduced by  $\sim 3$  dB. Interference that is two channels away is reduced by  $\sim 15$  dB. Rejection of signals removed by more than two channel bandwidths improves to better than 35 dB in all cases.

## IV. EXPERIMENTAL VERIFICATION

### A. Strong Continuous Artificial RFI With Cold Sky Background

The ADD radiometer was tested first with its antenna pointed at cold sky. RFI was introduced by locating a small dipole radiator near the aperture of the horn antenna. The dipole was connected to a continuous sinusoidal signal generator tuned to 1412 MHz and transmitting a power level of approximately 2000-K equivalent brightness temperature. Results of a 1-min duration series of measurements, with a 0.65 s integration time per sample, are shown in Figs. 3–6. Fig. 3 shows one sample of the discrete pdf measured in each of the eight frequency subbands. The pdfs in the outer subbands have classic “bell curve” shapes. The 1412-MHz RFI source is centered in subband #4, and its pdf is severely distorted.

In Fig. 4, the time series of  $T_B$  measured by each of the eight subbands is shown. The  $T_B$  in subband #4, which is centered on the artificial RFI source, is approximately 2000 K. The outer subbands (#1–2, 6–8) have RFI-free  $T_B$ s of approximately 40 K, which can be accounted for by integration of the antenna pattern over the angular distribution of incoming  $T_B$ . The inner subbands (#3 and 5) have  $T_B$  levels of 90–100 K, which is a composite of the natural antenna temperature plus out-of-band leakage of the strong RFI source through the band definition filters.

Fig. 5 shows the time series of normalized moment ratios for each of the subbands. The moment ratio is normalized by the average value measured while observing an RFI-free scene so that the presence of RFI will be indicated by significant deviations from a value of one. The ratio measured in subband #4 is approximately 0.59 as a result of the large RFI signal that is present. Subbands #3 and 5 have values near 0.98, which also differs from one but much less so. Ratios in the other subbands are all very close to one. A detailed examination of the behavior of the ratio as a function of the relative strengths of the sinusoidal and Gaussian distributed noise signals is presented in Section V.

Fig. 6 shows time series’ of the  $T_B$  reconstructed from the subbands in two ways. In the top panel, all eight subbands are averaged together, regardless of the level of RFI contamination. In the second panel, averages are taken over only those subbands for which the normalized moment ratio lies within three standard deviations of unity, where  $\sigma = 0.002$  is the standard deviation of the RFI-free normalized moment ratio. The third panel shows the difference between the first two panels and is

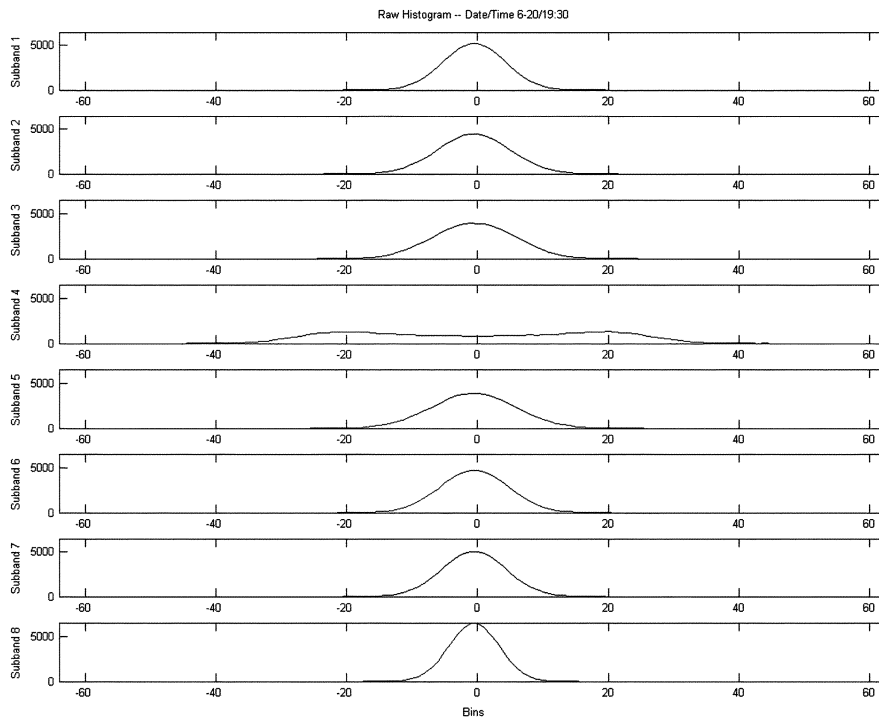


Fig. 3. Sample ADD measurement of the pdf of the signal entering the radiometer while viewing a continuous sine wave at 1412 MHz (centered on subband #4) added to background radiometric emission with the antenna pointed toward cold sky. The pdf is shown for each of the eight frequency subbands. The top panel is subband #1, and the bottom panel is subband #8. See Table III for the passband specifications of each subband. The  $x$  axis denotes “bin number” for each of 128 points in the discretely sampled pdf. The subband #4 pdf is clearly distorted away from a natural Gaussian distribution. There is also some distortion of subbands #3 and 5 that is not as evident.

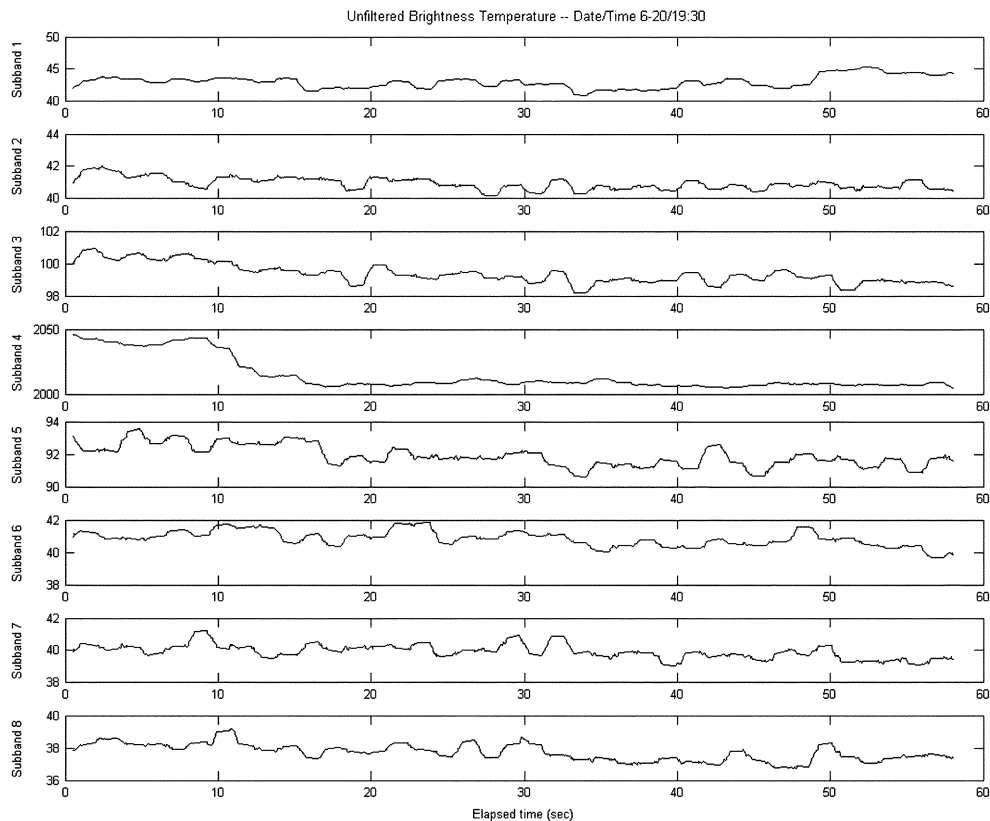


Fig. 4. ADD measurements over 1 min of the continuous sine wave plus background cold sky scene as in Fig. 3. Brightness temperature is shown versus time for each of the eight frequency subbands. The RFI is centered in subband #4, which exhibits a brightness temperature of  $\sim 2000$  K. Subbands #3 and 5 have 50–60-K levels of RFI due to the out-of-band rejection limitations of their filters. Subbands #1–2 and 6–8 are essentially free of RFI.

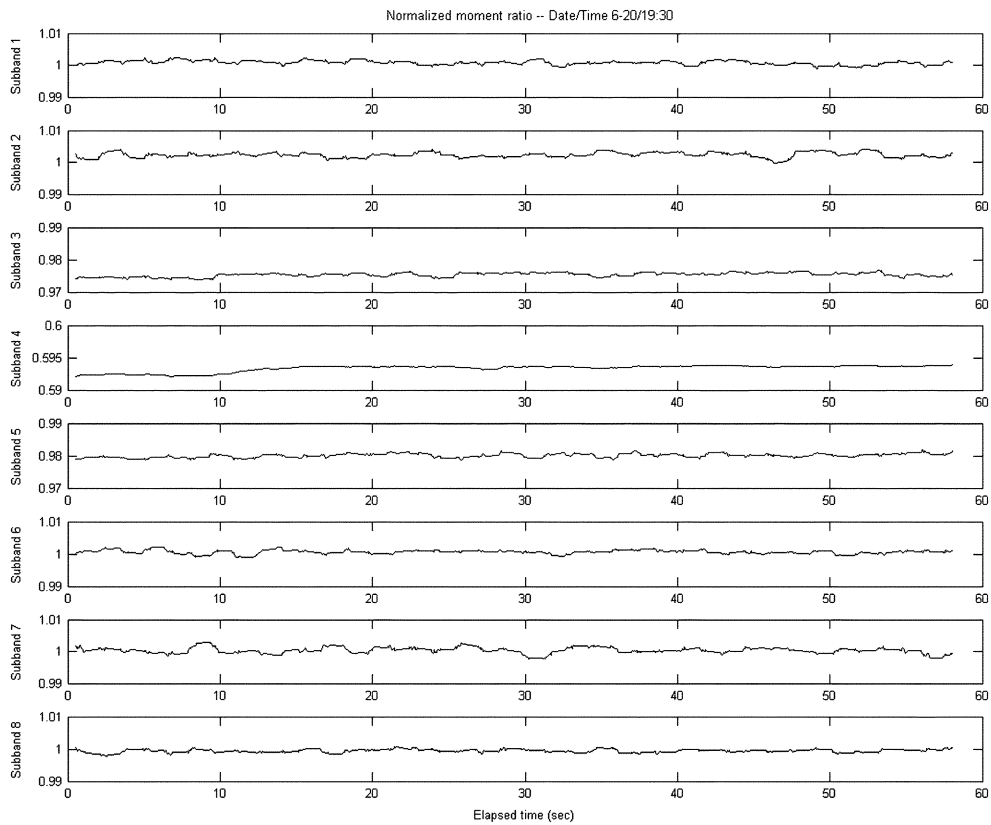


Fig. 5. ADD measurements as in Fig. 4. The normalized ratio between the fourth moment and the square of the second moment of the signal is shown for each of the eight frequency subbands. A normalized ratio of unity indicates that the signal has a Gaussian distributed amplitude consistent with natural thermal emission. The ratio for subband #4 is approximately 0.6 due to the strong sine wave present. Subbands #3 and 5 also have small nonunity ratios as a result of the RFI. The other subbands are RFI free. Note the scale change for subbands #3–5.

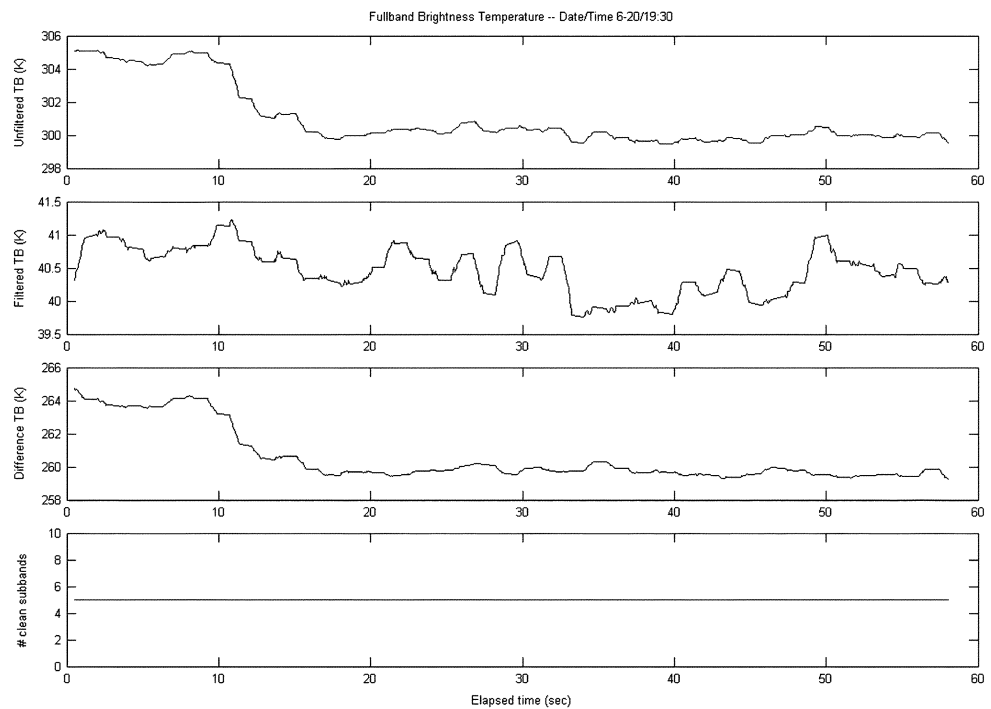


Fig. 6. ADD measurements as in Fig. 4. The top panel shows the full-band brightness temperature, averaged over all eight subbands. The second panel averages only those subbands for which the normalized moment ratio (shown in Fig. 5) is within three standard deviations of unity. The third panel is the differences between the two upper panels and is an indication of the level of RFI that is present. The bottom panel shows the number of RFI-free subbands. The mean level of the RFI signal in this case is  $\sim 260$  K.

an indication of the level of RFI that is present. The RFI signal contributes approximately 260 K to the full 24-MHz bandwidth

$T_B$ . The bottom panel shows the total number of subbands that were used to compute the RFI-free  $T_B$ . In all cases, subbands

TABLE III  
AVERAGE AND STANDARD DEVIATION OF ADD MEASUREMENTS  
OVER 1-min VIEWING LN<sub>2</sub> BLACKBODY LOAD PLUS  
~13-K PULSED SINE WAVE AT 1412 MHz

Frequency Sub Band (RF passband)	Brightness Temperature (K)	Normalized Moment Ratio
#1 (1401.5-1404.5 MHz)	121.39 ± 0.34	1.0003 ± 0.002
#2 (1404.5-1407.5 MHz)	122.30 ± 0.37	1.0004 ± 0.002
#3 (1407.5-1410.5 MHz)	122.86 ± 0.32	1.0066 ± 0.002
#4 (1410.5-1413.5 MHz)	135.48 ± 0.33	2.3466 ± 0.025
#5 (1413.5-1416.5 MHz)	123.91 ± 0.36	1.0078 ± 0.003
#6 (1416.5-1419.5 MHz)	122.27 ± 0.26	1.0001 ± 0.002
#7 (1419.5-1422.5 MHz)	122.64 ± 0.47	1.0010 ± 0.003
#8 (1422.5-1425.5 MHz)	122.55 ± 0.29	1.0005 ± 0.002

#3–5 were identified as contaminated and the number of clean subbands is 5.

### B. Weak Intermittent Artificial RFI With Cooled Blackbody Background

The ADD radiometer was next tested under more controlled laboratory conditions in order to examine the stability of the moment ratio and to assess its performance given lower level, intermittent RFI. The antenna was disconnected and replaced by an LN<sub>2</sub> cooled coaxial blackbody termination. A directional coupler was inserted between the LN<sub>2</sub> load and the radiometer so that artificial RFI signals could be added. The T<sub>B</sub> of the cold load, including losses and self-emission by the coupler and interconnecting cables, is estimated to be 122 K.

Measurements of the cold load alone, in the absence of any RFI, can be used to estimate the NEΔR uncertainty. The standard deviation of the individual samples of the normalized ratio gives an estimate of the NEΔR. For individual samples taken every 0.65 s, the normalized NEΔR is found to be 0.002 for each of the eight subband channels. This measurement can be compared to the theoretical value predicted by (7). The appropriate signal bandwidth to use in (7) is 3 MHz for each of the digital subband channels. The radiometer calibration sequence spends 44.4% of the time viewing each of the antenna and an ambient reference load and 11.2% of the time with the calibration noise diode added to each of these signals. Therefore, the appropriate integration time to use in the NEΔR expression is 44.4% of 0.65 or 0.289 s. The theoretical value for NEΔR is  $[24/(3 \times 10^6 * 0.289)]^{1/2} = 0.0053$ . This value must be divided by 3 to account for the normalization that gives an RFI-free ratio of 1. The resulting theoretical uncertainty is 0.0018, which is fairly close to the measured value of 0.002. The discrepancy may be due to the same types of secondary corrections that are typically made to the traditional radiometer NEΔT expression to account for short-term instrument instabilities.

To assess the detectability of radar-like RFI, a simulated radar signal was added to the cold load. The signal is a sine wave at 1412 MHz that is amplitude modulated by a pulse train with a 2-μs pulsewidth and a 360-Hz pulse repetition frequency. The power level of the unmodulated sine wave is set to approximately 18 000-K equivalent T<sub>B</sub>. With the 0.072% duty cycle of the pulse train, the effective T<sub>B</sub> of the radar signal is reduced to approximately 13 K. Results of a 1-min time series of measurements are summarized in Table III and illustrated in Figs. 7–9. Table III gives the average and standard deviation of T<sub>B</sub> and normalized moment ratio measured by each of the eight frequency subbands. Subband #4, which is centered on the RFI signal, has an average T<sub>B</sub> that is ~13 K higher than that of the other channels. Subbands #3 and 5 have average T<sub>B</sub>s that are approximately 0.4 K higher than channels #1–2 and 6–8. This is consistent with the out-of-band rejection expected of the filters. The standard deviation of T<sub>B</sub> is between 0.3 and 0.5 K for all eight channels. This standard deviation is a measure of the additive NEΔT noise present on each of the T<sub>B</sub> measurements. The normalized moment ratios listed in Table III indicate the presence of non-Gaussian distributed RFI in subbands #3–5. The ratio for subband #4 has an average value of 2.35, which is significantly higher than one. The ratios for subbands #3 and 5 are 1.007 and 1.008, respectively. The fact that these ratios are *higher* than one, whereas the ratios examined earlier with continuous sinusoidal RFI signals were *lower*, is addressed in Section V. The standard deviations of the ratios are sufficiently small (typically ~0.002) that the deviations from unity in subbands #3 and 5 are statistically significant. It is noteworthy that the change in T<sub>B</sub> due to RFI in subbands #3 and 5 is at the same level as the NEΔT of the measurements, yet it is clearly identifiable using the moment ratio test.

Fig. 7 shows the time series of T<sub>B</sub> measured by each of the eight subbands. Note that the T<sub>B</sub> in subband #4 has increased markedly as a result of the RFI. The small, step-like features apparent in Fig. 7 are artifacts of the calibration sequence that is used. Actual measurements are alternately made of the antenna signal and the ambient reference load at 0.729-s intervals. In the figure, only calibrated antenna samples are displayed and a running average is used to smooth across the reference load observations.

Fig. 8 shows the time series of normalized moment ratios for each of the subbands. Note that the time series of moment ratios for subbands #3 and 5, although noisy as a result of the NEΔR effect, nonetheless are consistently elevated above unity. Fig. 9 shows time series of the fullband T<sub>B</sub> (top panel) and the T<sub>B</sub> reconstructed with the RFI mitigation algorithm (second panel). The approximate 1.8-K difference between them, shown in the third panel, is an indication of the RFI level. It should be noted that a small residual correlation (explaining approximately 0.2 K of the variance in T<sub>B</sub>) is evident between the second and third panels in Fig. 9. This suggests that a small portion of the RFI signal is likely still present in the “RFI-free” panel—a result of leakage through the bandpass filters, imperfect RFI detection or, most likely, a combination of both. The bottom panel in Fig. 9 shows the number of clean subband channels, which varies between 5 and 6 since subband #4 is always rejected and subbands #3 and 5 are occasionally rejected.

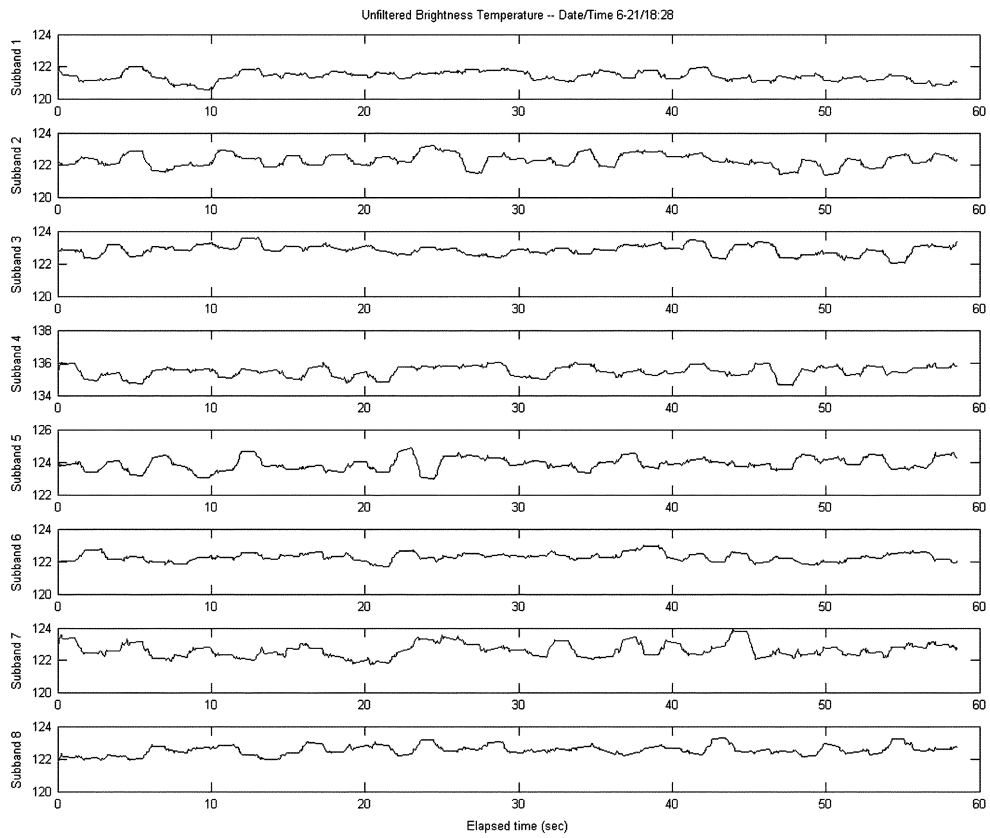


Fig. 7. ADD measurements over 1 min of an LN<sub>2</sub> cooled blackbody termination with an artificial radar signal added (pulsed sine wave at 1412 MHz, 2- $\mu$ s pulsewidth, 360-Hz PRF). Similar display as Fig. 4. The brightness temperature in subband #4 is approximately 13 K higher as a result of the radar-like signal.

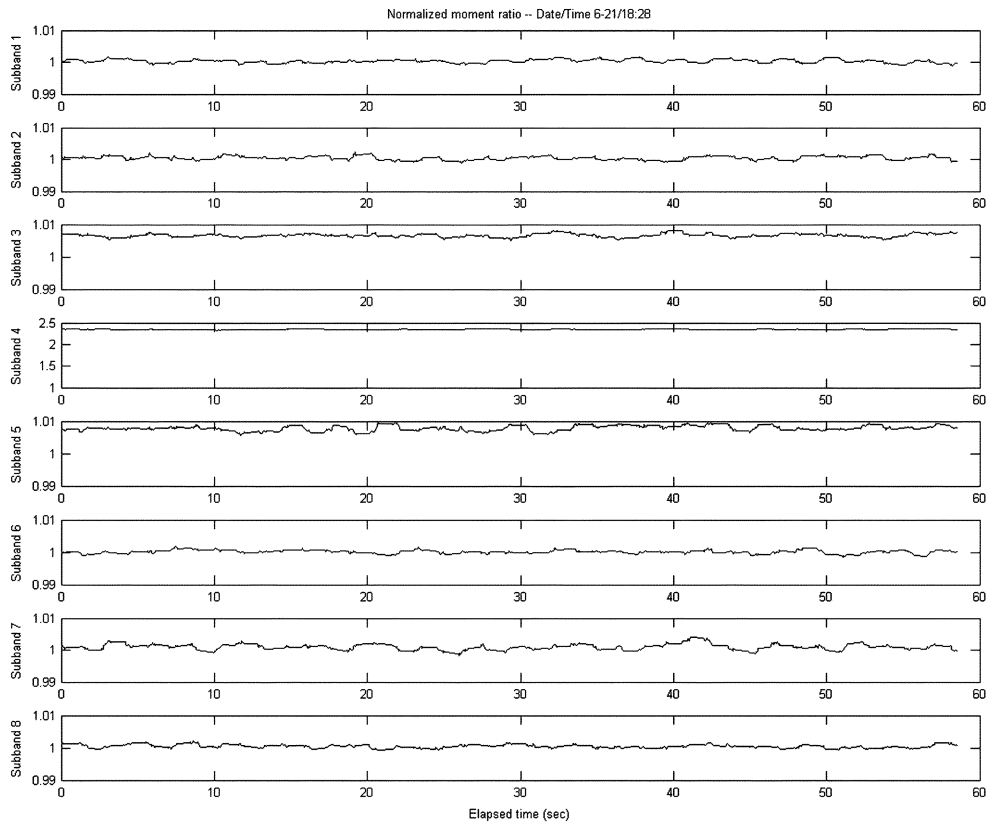


Fig. 8. ADD measurements as in Fig. 7. Similar display as Fig. 5. The ratio for subband #4 deviates significantly from unity due to the artificial radar signal. Subbands #3 and 5 also have small but significant indicators of RFI. Note the scale change for subband #4.

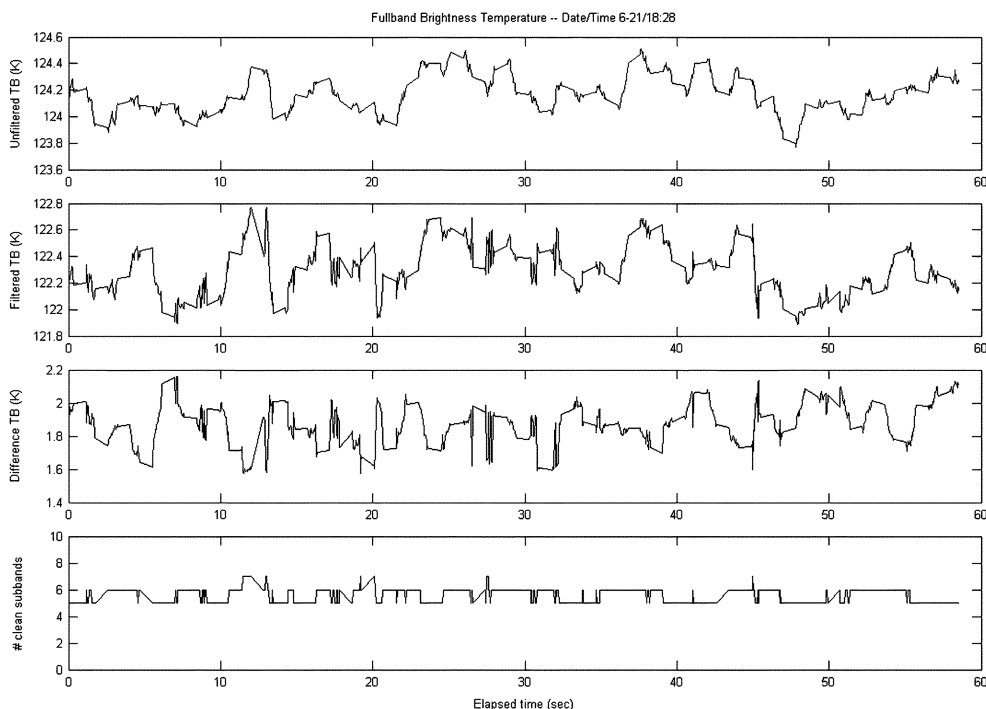


Fig. 9. ADD measurements as in Fig. 7. Similar display as Fig. 6. The mean level of the RFI signal in this case is  $\sim 1.8$  K.

### C. Air Traffic Control Radar With Horizon Background

The ADD radiometer was operated in close proximity to an ARSR-1 commercial air traffic control radar located in Canton, MI (N42 16' 36", W083 28' 27"). The ARSR-1 transmits at approximately 1305 MHz with a peak transmit power of 4 MW, pulsewidth of 2  $\mu$ s, and pulse repetition frequency of 360 Hz. The radar rotates in azimuth at a rate of approximately 10 s per revolution. The radiometer's frequency downconversion is performed with a local oscillator operating at 1386.5 MHz. This results in an IF center frequency for the radar signal of 81.5 MHz. The digitizer used by the ADD operates at a sample rate of 110 MHz. This places an aliased response to the radar signal at 28.5 MHz, i.e., centered in subband #5. Although there are image reject and band definition filters associated with the downconversion stage, as well as an antialiasing filter prior to the digitizer, a small remnant of the extremely strong radar signal is still present in the ADD samples.

The ADD radiometer was deployed at a height of 15 m approximately 150 m north of the radar with the radiometer antenna pointed to the north at an elevation angle of  $0^\circ$  (i.e., toward the horizon and away from the radar). The  $20^\circ$  radiometer antenna field of view contained a grassy field in the foreground, a line of trees located several hundred meters away, and the clear sky above them. A 1-min sample of the ADD measurements is shown in Figs. 10–12. Fig. 10 shows the time series of individual  $T_B$ s measured in each of the eight subbands. The  $T_B$ , which varies with frequency between 174 and 180 K, is generally consistent with an antenna field of view that is partially filled by sky and by the grassy field and trees. Fig. 11 shows the time series of normalized moment ratios for each of the subbands. The 10-s per revolution azimuth scan rate of the radar is clearly evident in subband #1 as periodic increases in the moment ratio at an elapsed time of 1, 11,  $\dots$ , 51 s. It is likely that the radar signal is

entering the radiometer via backscatter from the tree line to the north of the radiometer. The normalized moment ratio in subbands #4 and 5 is generally much higher than unity. The level of RFI is expected to be highest in these bands due to the frequency aliasing discussed above. The fact that these subbands do not exhibit such a clear 10-s periodicity is likely due to the many ground clutter targets that were present at other azimuth angles. Subbands #6–8 appear to be least affected by the radar.

Fig. 12 shows the time series of TB reconstructed with and without the RFI mitigation algorithm. The third panel shows the difference between them, which is the total contribution to the TB from the radar. That contribution ranges between 0 and 1.0 K. The fact that the RFI contamination is so low when operating in the immediate vicinity of a 4-MW radar transmitter is at least in part due to the very low backlobes of the horn antenna and to the very high out-of-band rejection of the radiometer's analog band definition filter. The bottom panel in Fig. 12 tallies the number of subbands that were considered free of RFI. In most cases, two out of eight subbands (#4 and 5) were corrupted, with a third subband (#1) additionally tagged as corrupted only during the periodic pulses every 10 s. These results corroborate those of the controlled laboratory tests presented above. Air traffic control radar RFI at the level of the  $NE\Delta T$  of the brightness temperature measurements can be confidently detected and removed by the ADD system.

### V. DEPENDENCE OF MOMENT RATIO ON SINUSOIDAL RFI SIGNALS

Numerical simulations were performed to examine the response of the normalized moment ratio to pulsed and continuous sinusoidal RFI of the sort encountered in the tests described in Section IV. Radiometric noise was generated by a Gaussian random number generator with a fixed standard deviation of 10

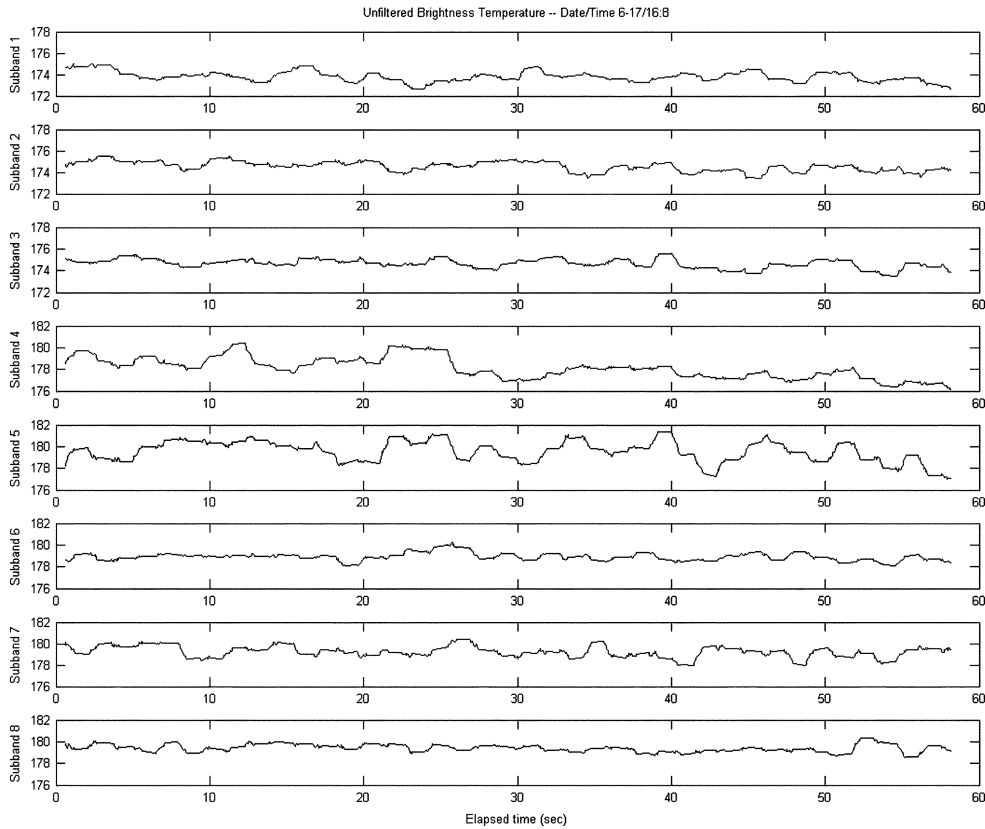


Fig. 10. ADD measurements over 1 min while observing a tree line along the horizon near an ARSR-1 air traffic control radar. Similar display as Fig. 4. ARSR-1 operates at 1305 MHz, well below the operating frequency range of the radiometer, and so its presence as RFI is not obvious in this figure.

(consistent with ADD measurements such as those shown in Fig. 3). A sinusoidal signal at frequency 25.5 MHz was added to the noise (consistent with a 1412-MHz ADD input signal, after frequency downconversion). The sinusoid was gated by 2- $\mu$ s pulses. The duty cycle of the pulses and the amplitude of the sinusoid were varied parametrically to evaluate their effect on the moment ratio. The signal was sampled at 13.75 MHz by a seven-bit bipolar digitizer covering the input range  $-63$  to  $+64$  (consistent with the ADD digitizer after subband sample decimation). A total of 900 000 realizations were generated (consistent with the ADD time-bandwidth product), from which the normalized moment ratio was computed. The results are shown in Fig. 13. The  $y$  axis in the figure is the normalized moment ratio. The  $x$  axis, labeled SNR, is the ratio between the variance of the sinusoid and that of the Gaussian noise signal. This corresponds to the relative  $T_B$  of the two signals. For example, a signal-to-noise ratio (SNR) of  $-10$  dB corresponds to a sinusoidal signal that would raise the RFI-free  $T_B$  by 10%. An SNR of  $+10$  dB would raise it by 1000%.

In curve (a) of Fig. 13, the duty cycle of the sinusoid is fixed at 1% and its amplitude is varied. The normalized moment ratio begins to rise above one as the SNR increases above  $-40$  dB. For values of the SNR above 5–10 dB, corresponding to very high amplitude sinusoids, the moment ratio saturates at a value of approximately 3.4. The saturation is caused by the seven-bit digitizer, which “pins” at signal amplitudes of  $-63$  and  $+64$ . The fact that the moment ratio increases with the amplitude of the RFI can be appreciated by considering the effect that the

RFI has on the composite pdf of the two signals. The pdf for the amplitude of a sinusoidal signal  $x(t) = A\sin(\omega t)$  is given by

$$p_S(x) = \frac{1}{\pi\sqrt{A^2 - x^2}}, \quad \text{for } |x| < A. \quad (8)$$

The pdf for the amplitude of natural radiometric emission is Gaussian, or

$$p_G(x) = \frac{1}{\sigma\sqrt{2\pi}}e^{-(x^2/2\sigma^2)}. \quad (9)$$

The sinusoidal pdf in (8) has its minimum at  $x = 0$  and increases as the magnitude of  $x$  approaches  $A$ . A Gaussian distribution, on the other hand, is peaked at its center and decreases as the magnitude of  $x$  increases.

A composite pdf, representing the combined signals, is formed by the weighted average

$$p_C(x) = dp_{GS}(x) + (1 - d)p_G(x) \quad (10)$$

where  $d$  is the duty cycle of the pulsed sinusoid and  $p_{GS}(x)$  is the pdf for the sum of the sinusoid and the noise signal. In general,  $p_{GS}(x)$  is given by the convolution of (8) with (9). For very large amplitude sinusoids, and in particular for cases where the ADD digitizer is at or near saturation,  $p_S(x)$  will become highly localized near  $x = \pm A$ . In this case, the convolution of (8) with (9) will largely reposition  $p_G(x)$  in the vicinity of  $x = \pm A$ . The weighted average in (10) will, then, produce

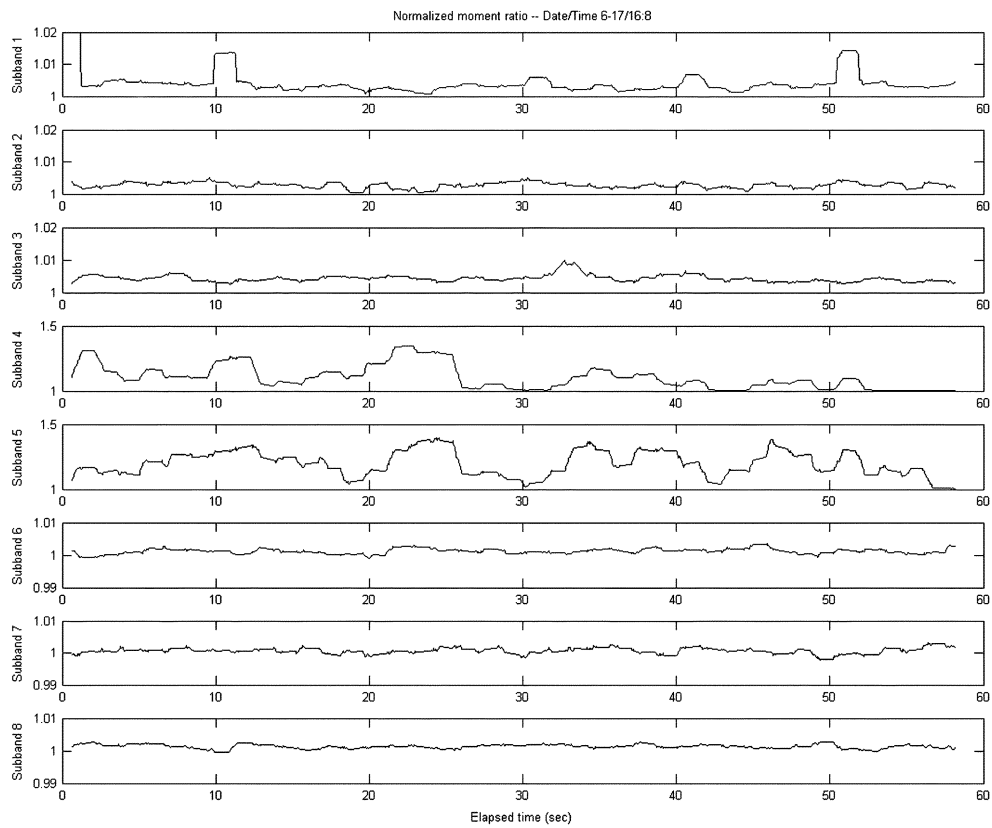


Fig. 11. ADD measurements as in Fig. 10. Similar display as Fig. 5. The ARSR-1 azimuth sweep rate of 10 s per revolution is evident in subband #1 as a periodic deviation of the signal statistics from purely Gaussian. Subbands #4 and 5 are much more strongly and persistently affected by RFI because the radar signal is aliased into this portion of the RF spectrum by the sampling strategy of the ADD. Subbands #6–8 are largely unaffected by the radar. Note scale changes between subbands #1–3, 4–5, and 6–8.

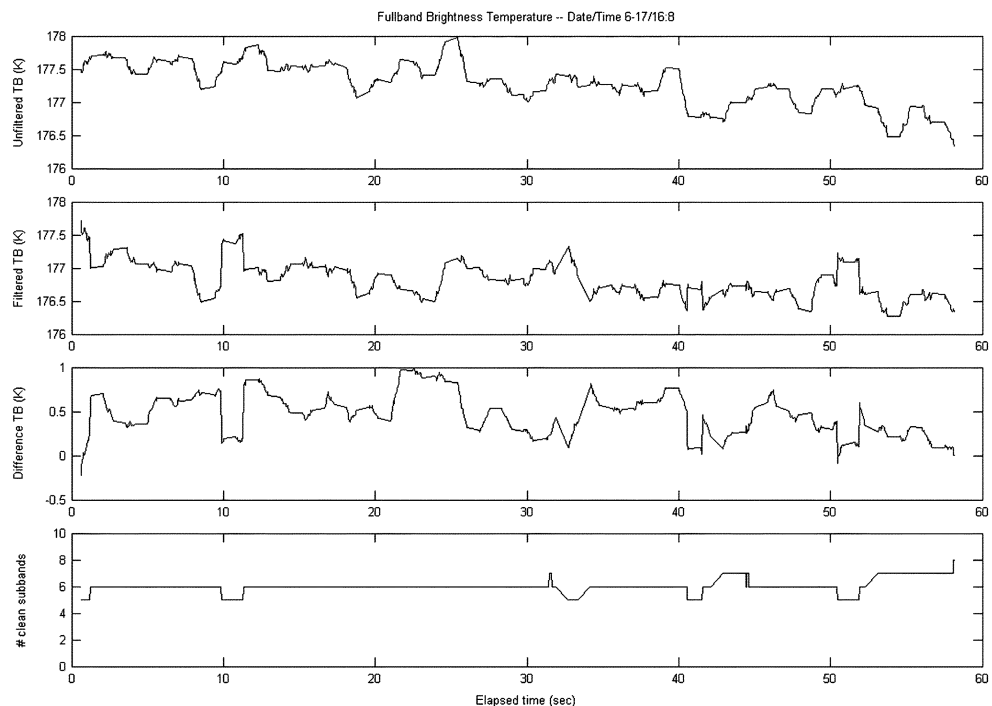


Fig. 12. ADD measurements as in Fig. 10. Similar display as Fig. 6. ARSR-1 radar contamination of the brightness temperature, noted in the third panel, varies over approximately 0–1 K. The contamination is largely removed by the subband mitigation algorithm.

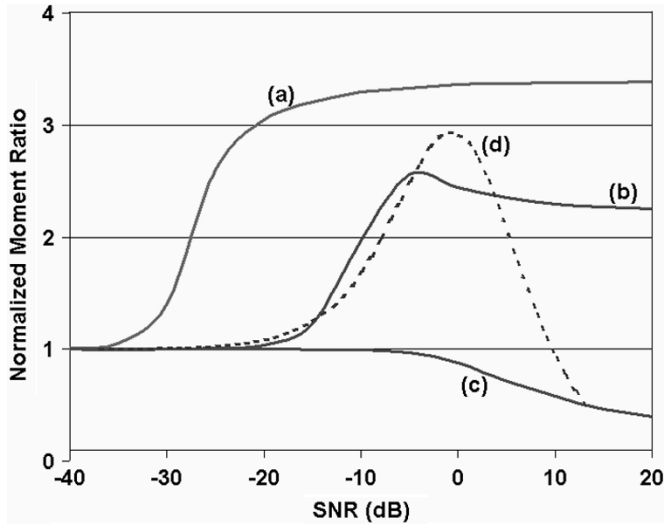


Fig. 13. Numerical simulation of the dependence of the normalized moment ratio on the strength of pulsed ( $2\text{-}\mu\text{s}$  pulse width) sinusoidal RFI with (a) 1% duty cycle and variable amplitude, (b) 10% duty cycle and variable amplitude, (c) 100% duty cycle (i.e., continuous wave) and variable amplitude, or (d) fixed amplitude and variable duty cycle. SNR is the ratio between the variance of the sinusoid and of the Gaussian noise signal, which corresponds to the relative brightness temperature of the two signals.

three superposed Gaussian distributions, one centered at  $x = 0$  with weight  $(1 - d)$  and two in the vicinity of  $x = \pm A$ , each with weight  $d/2$ . This deformation of the Gaussian distribution is an example of the “heavy tails” that are known to raise its kurtosis [5].

Curve (b) of Fig. 13 assumes a fixed duty cycle of 10% for the pulsed sinusoid while its amplitude is varied to affect the SNR. The effect of the signal on the moment ratio does not become noticeable until the SNR exceeds  $-25$  dB. This decrease in sensitivity to RFI, relative to a 1% duty cycle, results because, with the higher duty cycle, a smaller amplitude sinusoid is required to produce a given SNR. With a smaller amplitude,  $A$ , the pdf,  $p_{GS}(x)$ , will be localized near points  $x = \pm A$  that are not so far out on the tails of  $p_G(x)$ . This reduces their impact on the kurtosis.

Curve (c) of Fig. 13 assumes a duty cycle of 100% for the sinusoid (i.e., a continuous signal). The normalized moment ratio for a sinusoid alone is exactly one half. In the figure, the ratio can be seen to drop monotonically from one toward one half as the amplitude of the sinusoid increases. At very high amplitudes, it decreases below one half due to distortion resulting from saturation of the seven-bit digitizer. It is noteworthy that the moment ratio is markedly less sensitive to RFI from a continuous than a pulsed sinusoid.

The fact that the moment ratio increases for low values of the duty cycle but decreases with a duty cycle of 100% implies that there is some intermediate duty cycle for which the moment ratio will be unchanged and, hence, insensitive to RFI. This condition is assessed in curve (d) of Fig. 13, which plots the moment ratio assuming a constant amplitude sinusoid but variable duty cycle. The amplitude is fixed at 64, which corresponds to the dynamic range of the ADD digitizer. At very low values of SNR (and of duty cycle), the moment ratio increases above one. The ratio reaches a peak of 2.9 at an SNR slightly below 0 dB

(duty cycle = 4%) and then begins to decrease. The ratio passes through one at an SNR of 10 dB (duty cycle of 50%) and then decreases further. Thus, there is a “blind spot” in detection of the pulsed sinusoidal signal if the duty cycle is near 50%.

## VI. CONCLUSION AND DISCUSSION

An agile digital detector has been developed to detect and remove RFI from microwave radiometer measurements. It directly measures the discrete probability density function of the amplitude of the radiometer signal. The square-law detection that is typically performed by a conventional radiometer can be replicated in postprocessing by computing the second moment of the pdf. Higher order moments can also be computed in postprocessing, and this opens the door to a new class of RFI detection algorithms. One such algorithm, based on the ratio between the fourth moment and the square of the second moment, has been shown to be very stable when RFI is not present but quite responsive to the presence of low-level RFI. Pulsed sinusoidal RFI signals originating from an air traffic control radar can be reliably detected with brightness temperatures as low as the  $NE\Delta T$  uncertainty in the radiometer measurements. The ADD also includes a bank of digital filters which divide up the full radiometer bandwidth into well-isolated subbands. This allows the RFI to be filtered out by only using those subbands that have “passed” the RFI detection test. These results should be qualified on two counts. The moment ratio test was found to be insensitive to sinusoidal RFI signals with a duty cycle of 50%. Fortunately, the sensitivity increases markedly at lower duty cycles where radars tend to operate. In addition, other potential sources of RFI, having nonsinusoidal amplitude probability distributions, will likely have different effects on the measured pdf and may well be more difficult to detect. This is an area under current investigation by the authors.

The ADD can be considered “agile” in several senses. It can act as a conventional square-law detector by computing the second moment of the pdf of a signal. It can detect the presence of non-Gaussian distributed signals using the moment ratio method described above. Because the pdf of the signal is directly measured, it is also amenable to many other possible RFI detection and identification algorithms that have yet to be developed—perhaps based on other statistics of the signal. The ADD digital filter bank makes RFI mitigation agile by adaptively selecting and removing contaminated subbands. The fact that the predetected radiometer signal has been digitized and made available for high-speed, real-time digital signal processing in an FPGA DSP module also opens up numerous other possibilities. For example, the radiometer used in this study featured dual linearly polarized channels, both of which were digitized and available for processing. All of the results presented above are from observations at a single, vertical, polarization, but the horizontally polarized signal was also simultaneously available. This permits the two signals to be digitally cross-correlated and the third and fourth Stokes  $T_B$  to be generated. Relative to the other, pdf-related, functions of the ADD, generation of the third and fourth Stokes channels is straightforward and not particularly firmware intensive. For this reason, any reasonably well-designed ADD backend should

be able to provide square-law detection, RFI detection and mitigation, and fully polarimetric operation.

#### ACKNOWLEDGMENT

The authors would like to acknowledge the valuable assistance of R. De Roo, D. Boprie, B. Lim, and H. Elsaadi (University of Michigan) and B. Hornbuckle (Iowa State University), with the Canton, MI field campaign. Comments by the anonymous reviewers were insightful and contributed to the results.

#### REFERENCES

- [1] P. A. Dirmeyer, F. J. Zeng, A. Ducharme, J. C. Morrill, and R. D. Koster, "The sensitivity of surface fluxes to soil water content in three land surface schemes," *J. Hydrometeorol.*, vol. 1, no. 2, pp. 121–134, 2000.
- [2] A. J. Gasiewski, M. Klein, A. Yevgrafov, and V. Leuski, "Interference mitigation in passive microwave radiometry," *Proc. IGARSS*, vol. 3, pp. 1682–1684, Jun. 24–28, 2002.
- [3] F. J. Harris, *Multirate Signal Processing*. Upper Saddle River, NJ: Prentice-Hall, 2004.
- [4] J. T. Johnson, G. A. Hampson, and S. W. Ellingson, "Design and demonstration of an interference suppressing microwave radiometer," in *Proc. IGARSS*, vol. 3, Anchorage, AK, Sep. 20–24, 2004, pp. 1683–1686.
- [5] J. F. Kenney and E. S. Keeping, "Kurtosis," in *Mathematics of Statistics*, 3rd ed. Princeton, NJ: Van Nostrand, 1962, ch. 1, Sec. 7.12, pp. 102–103.
- [6] G. M. P. Kempen and L. J. Vliet, "Mean and variance of ratio estimators used in fluorescence ratio imaging," *Cytometry*, vol. 39, pp. 300–305, 2000.
- [7] D. M. Le Vine and M. Haken, "RFI at L-band in synthetic aperture radiometers," in *Proc. IGARSS*, vol. 3, Toulouse, France, Jul. 21–25, 2003, pp. 1742–1744.
- [8] D. M. Le Vine, "ESTAR experience with RFI at L-band and implications for future passive microwave remote sensing from space," in *Proc. IGARSS*, vol. 2, Toronto, ON, Canada, Jun. 24–28, 2002, pp. 847–849.
- [9] L. Li, E. G. Njoku, E. Im, P. Change, and K. St. Germain, "A preliminary survey of radio-frequency interference over the U.S. in Aqua AMSR-E data," *IEEE Trans. Geosci. Remote Sens.*, vol. 42, no. 2, pp. 380–390, Feb. 2004.
- [10] R. A. Losada, "Design finite impulse response digital filters," *Microw. RF*, Apr. 2004. Article ID 7965.
- [11] E. G. Njoku and L. Li, "Retrieval of land surface parameters using passive microwave measurements at 6 to 18 GHz," *IEEE Trans. Geosci. Remote Sens.*, vol. 37, no. 1, pp. 79–93, Jan. 1999.
- [12] E. G. Njoku, P. Ashcroft, T. K. Chan, and L. Li, "Global survey and statistics of radio-frequency interference in AMSR-E land observations," *IEEE Trans. Geosci. Remote Sens.*, vol. 43, no. 5, pp. 938–947, May 2005.
- [13] M. Regner, N. S. Chauhan, and D. B. Kunkee, "NPOESS Conical Microwave Imager Sounder: RFI issues and progress," in *Proc. IGARSS*, vol. 4, Anchorage, AK, Sep. 20–24, 2004, pp. 2443–2445.
- [14] C. Ruf and C. Principe, "X-band lightweight rainfall radiometer first light," in *Proc. IGARSS*, Toulouse, France, Jul. 21–25, 2003.



**Christopher S. Ruf** (S'85–M'87–SM'92–F'01) received the B.A. degree in physics from Reed College, Portland, OR, and the Ph.D. degree in electrical and computer engineering from the University of Massachusetts, Amherst.

He is currently a Professor of atmospheric, oceanic, and space sciences and electrical engineering and computer science at the University of Michigan, Ann Arbor. He has worked previously as a Production Engineer for Intel Corporation, Santa Clara, CA, as a member of the technical staff for the Jet Propulsion Laboratory, Pasadena, CA, and as a member of the faculty at Pennsylvania State University, University Park. During 2000, he was a Guest Professor at the Technical University of Denmark, Lyngby. His research interests involve microwave remote sensing instrumentation and geophysical retrieval algorithms. He is currently involved with spaceborne radiometers on the current TOPEX, GeoSat Follow-on, Jason, and WindSat and the upcoming CMIS, Aquarius, and Juno missions. He has published over 87 refereed articles and is a past Associate Editor and Guest Editor for *Radio Science*.

Dr. Ruf has received three NASA Certificates of Recognition and four NASA Group Achievement Awards, as well as the 1997 GRS-S Transactions Prize Paper Award and the 1999 IEEE Judith A. Resnik Technical Field Award. He is a past Editor of the IEEE GRS-S Newsletter and currently an Associate Editor and Guest Editor of the IEEE TRANSACTIONS ON GEOSCIENCE AND REMOTE SENSING. He is a member of the AGU, AMS, and URSI Commission F.



**Steven Gross** received the B.S. and M.S. degrees in electrical engineering and the M.B.A. degree from Michigan State University, East Lansing, in 1990, 1993, and 2000, respectively.

He is currently a member of the engineering staff of the Space Physics Research Laboratory (SPRL), University of Michigan. Prior to joining SPRL, he was a member of technical staff in the High Energy Physics Group, Michigan State University and at the TRW Corporation. His primary engineering activities involve high-speed digital logic and field-programmable gate array design.

Mr. Gross is the recipient of a 2004 NASA Group Achievement Award as a member of the Lightweight Rainfall Radiometer Instrument Team.



**Sidharth Misra** received the B.E. degree in electronics and communication from Nirma Institute of Technology, Gujarat University, Ahmedabad, India, in 2004. He is currently pursuing the M.S. degree at the University of Michigan, Ann Arbor.

He is at present a Graduate Student Research Assistant in the Space Physics Research Laboratory, University of Michigan. He has previously worked for the Space Application Center, Indian Space Research Organization, Ahmedabad, on the design and implementation of a digital subsystem for the Oceansat-II scatterometer module. He is currently involved with the agile digital detector for RFI mitigation. His research interests involve signal detection and estimation, filter design, and image processing.